Electronic Supplementary Material (ESI) for Chemical Communications.

Atomic controllable anchoring of uranium into zirconate pyrochlore with ultrahigh loading capacity

*Jian Sun[ab], Jing Zhou[a], Lili Li[a], Zhiwei Hu[c], Ting-Shan Chan[d], Tonya Vitova[e], Sanzhao Song[a], Renduo Liu[a], Chao Jing[a], Haisheng Yu[a], Ming Zhang[f], Joerg Rothe [*e], Jian-Qiang Wang[*ab], Linjuan Zhang [*ab]*

[a]*Key Laboratory of Interfacial Physics and Technology, Shanghai Institute of Applied Physics, Chinese Academy of Sciences, Shanghai 201800, China.*

[b]*University of Chinese Academy of Sciences, Beijing 100049, China.*

[c]*Max Planck Institute for Chemical Physics of Solids, Nöthnitzer Strasse 40, 01187 Dresden, Germany.*

[d]*National Synchrotron Radiation Research Center, 101 Hsin-Ann Road, Hsinchu 30076, Taiwan.*

[e]*Karlsruhe Institute of Technology (KIT), Institute for Nuclear Waste Disposal (INE), Karlsruhe 76021, Germany.*

[f]*Institute of Nuclear Science and Technology, Sichuan University, Chengdu 610064, China.*

1. Materials and supplies

All of the chemicals were of analytical grade and were used as received without further purification. The reagents used in this experiment contained $La(NO_3)_3 \cdot 6H_2O$ (99.9%), $ZrO(NO_3)_2 \cdot xH_2O$ (99.5%), $UO_2(NO_3)_2 \cdot 6H_2O$, NH_4OH (28%), $NaNO_3$ (99.9%) and KNO_3 (99.9%).

2. Synthesis

$La_2Zr_2O_7$ was synthesized by using a molten salt method and solid-state method. For the molten salt method (Scheme S1), which is described elsewhere [1]. First, 5 mmol $La(NO_3)_3 \cdot 6H_2O$ and 5 mmol $ZrO(NO_3)_2 \cdot xH_2O$ were added to 18 MΩ ultrapure water and configured as a 200 mL homogeneous solution. Then, 200 mL of dilute ammonia (NH_4OH:H_2O = 1:9 (v/v)) solution was dropped into the mixed solution while stirring. The colloidal precursor mixture was centrifuged and transferred to a vacuum drying box at 55 °C for 72 h to obtain the bulk composite precursor. The precursor and certain composite nitrate molten salts ($NaNO_3$:KNO_3 = 1:1 (molar ratio)) were mixed and then calcined at 750 °C for 6 h. After cooling, the product was washed with 18 MΩ ultrapure water several times and transferred to a vacuum drying box at 55 °C for 12 h to obtain the final $La_2Zr_2O_7$ powder. For the solid-state method, $La(NO_3)_3 \cdot 6H_2O$ and $ZrO(NO_3)_2 \cdot xH_2O$ were dissolved in 18 MΩ deionized water and stirred at 110 °C to evaporate the water. Then, the mixtures were heated at 700 °C for 10 h, ground for 15 minutes and pressed into pieces. Finally, they were calcined at 1440 °C for 48 h to obtain the $La_2Zr_2O_7$ product. Similarly, U-doped $La_2Zr_2O_7$ products were prepared by replacing $La(NO_3)_3 \cdot 6H_2O$ or $ZrO(NO_3)_2 \cdot xH_2O$ with $UO_2(NO_3)_2 \cdot 6H_2O$ in stoichiometric amounts.

3. Characterization

The crystal structure was examined by X-ray diffraction spectroscopy (XRD) on a Bruker D8 advanced AXS diffractometer with Cu Kα irradiation and micro-Raman spectroscopy (Horiba LabRAM HR Evolution with laser wavelength of 633 nm). The element ratio was detected by high resolution inductively coupled plasma-mass spectrometry (HR-ICP-MS, Attom, Nu Instruments, UK). Synchrotron X-ray diffraction spectra were also collected at beamline 01C2 of the National Synchrotron Radiation Research Center (NSRRC), Taiwan. The morphology was characterized by transmission electron microscopy (TEM, FEI Tecnai G2 F20 S-TWIN) and high-angle annular dark-field scanning transmission electron microscopy (HAADF-STEM, JEM-ARM200F, the convergent angle of the electron beam was 25 mrad). Raman spectra were collected using a confocal microscope (Horiba LabRAM HR Evolution) with an excitation wavelength of 633 nm and a 50× long working distance objective. Spectral shifts were calibrated routinely against the value of a silicon wafer (520.7 cm^{-1}). Conventional U L_3-edge and Zr K-edge X-ray absorption spectra (XAS) were collected at the 07A1 beamline of the National Synchrotron Radiation Research Center (NSRRC) in Taiwan and BL14W1 of Shanghai Synchrotron Radiation Facility (SSRF). U-M_4 XAS was collected in both fluorescence mode at beamline 16A1 of NSRRC and transmission mode using an in-house laboratory-based X-ray absorption spectrometer. High-resolution partial fluorescence detection (HERFD) X-ray absorption near-edge structure (XANES) of the U M_4-edge was performed at the CAT-ACT beamline at the KARA storage ring, KIT synchrotron light source, Karlsruhe, Germany.

4. Computational details

First principles calculations were employed by the Vienna ab initio Simulation Package (VASP) [2, 3] to implement DFT in conjunction with the projector augmented wave (PAW) formalism. The

exchange-correlation term was modelled using the General Gradient Approximation (GGA) with Perdew-Burke-Ernzerhof (PBE) [4]. Consequently, the O $2s^2 2p^4$, La $4d^{10} 5d^1$, Zr $4d^2 5s^2$, and U $6p^6 7s^2 6d^1 5f^3$ states are treated as valence electrons. The electronic wave functions are expanded in plane waves using an energy cut-off of 500 eV. The force and energy convergence criteria were set to 0.02 eV/Å and 10^{-6} eV, respectively, and 3×3×3 Monkhorst–Pack [5] k-point meshes were employed to sample the Brillouin zones in all calculations. The defect formation energy (E_d) for defect X with charge state q is dependent on the Fermi-level position according to [6, 7]:

$$E_d(X^q) = E^{total}(X^q) - E^{total}(pristine) + \sum_i n_i \mu_i + q(E_F + E_v + \Delta V) \quad (1)$$

where $E^{total}(X^q)$ is the total energy obtained from a supercell with the doping ion X of charge state q, and $E^{total}(pristine)$ is the total energy of the supercell without any doping ions. n_i indicates the number of atoms of species i that have been added or removed during the doping process, and μ_i is the corresponding chemical potential. The detailed calculation equations and stability range of μ_i are described as in "**The chemical potential calculations**" below. E_F is the Fermi level with respect to the pristine valence band maximum (VBM) E_v, and ΔV aligns the electrostatic potentials in the doping supercell with that in the pristine material.

5. Structural analysis of the sample with fully substitution of Zr with U

For the sample with fully substitution of Zr with U, we carefully checked its composition and structure through ICP-MS, XRD, Raman, XAS and HAADF-STEM characterizations. To determine the precise cation ratio, ICP-MS experiments were carried out and showed that the element configuration of U/La is 0.785, which is close to the result of SEM-EDS. Considering the valence state of $La^{3+}$and U^{6+} confirmed by XAS, the sample should be $La_2U_{1.57}O_{7.71}$. Based on the

Lab- and Synchrotron-based XRD analysis, the space group of $La_2U_{1.57}O_{7.71}$ sample corresponds to Fm-3m, supporting the defective fluorite phase. Raman spectroscopy analysis also confirmed this point, in which only single broad Raman active mode in the range of 200-600 cm^{-1} can be observed. We also examined the atomic arrangement of $La_2U_{1.57}O_{7.71}$ sample using a high-angle annular-dark-field scanning transmission microscope (HAADF-STEM). Fig. S5 shows the HAADF-STEM images viewed down the [211] axis of $La_2Zr_2O_7$ sample (pyrochlore phase), as well as the $La_2U_{1.57}O_{7.71}$ sample. Since La^{3+} (1.16 Å, 8-fold coordination) and Zr^{4+} (0.72 Å, 6-fold-coordination) have different ionic radius, the ordered arrangement structure of pyrochlore phase in $La_2Zr_2O_7$ sample can be confirmed as shown in Fig. S5a-b. There are no obvious differences in atomic arrangement between $La_2Zr_2O_7$ and $La_2U_{1.57}O_{7.71}$ samples, supporting that the $La_2U_{1.57}O_{7.71}$ sample would be isostructural with the pyrochlore phase. In the fluorite phase, there is an equal occupancy of A and B cations on the cation sublattice, and therefore no obvious radius differences as shown in Fig. S5c-d supports the fluorite phase in $La_2U_{1.57}O_{7.71}$ sample.

6. the speciation of U(VI)

The possibility of uranium in U(VI) speciation can be evaluated through the comparisons of XANES spectra for the U doped $La_2Zr_2O_7$ samples and other uranium group references in Fig. S7b. The fine structure around the absorption edge generally comprises the contribution from multiple-scattering resonances of the photoelectrons around absorbing atom. The white line at the U L_3-edge originates from transitions from $2p_{3/2}$ core hole to unoccupied 6d states, and is very sensitive to the local coordination chemistry of the absorbing atom [8]. The significant differences between the spectra of all samples and references rules out the possibility of uranium being present in the form of UO_4^{2-}, UO_2^{2+} and UO_3 in the U doped $La_2Zr_2O_7$ samples. This indicated the presence of uranium as uranate UO_6^{6-} in both A-site and B-site doped $La_2Zr_2O_7$ samples.

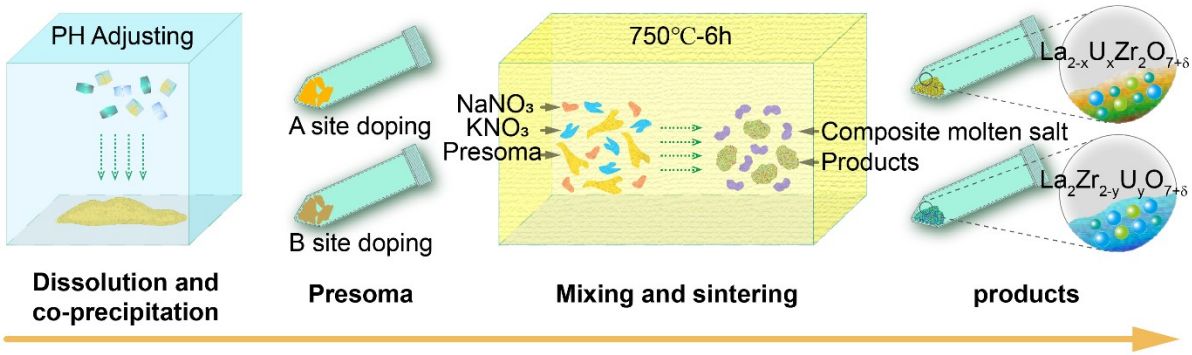

Scheme S1 The synthesis of U-doped $La_2Zr_2O_7$ powder using molten salt method.

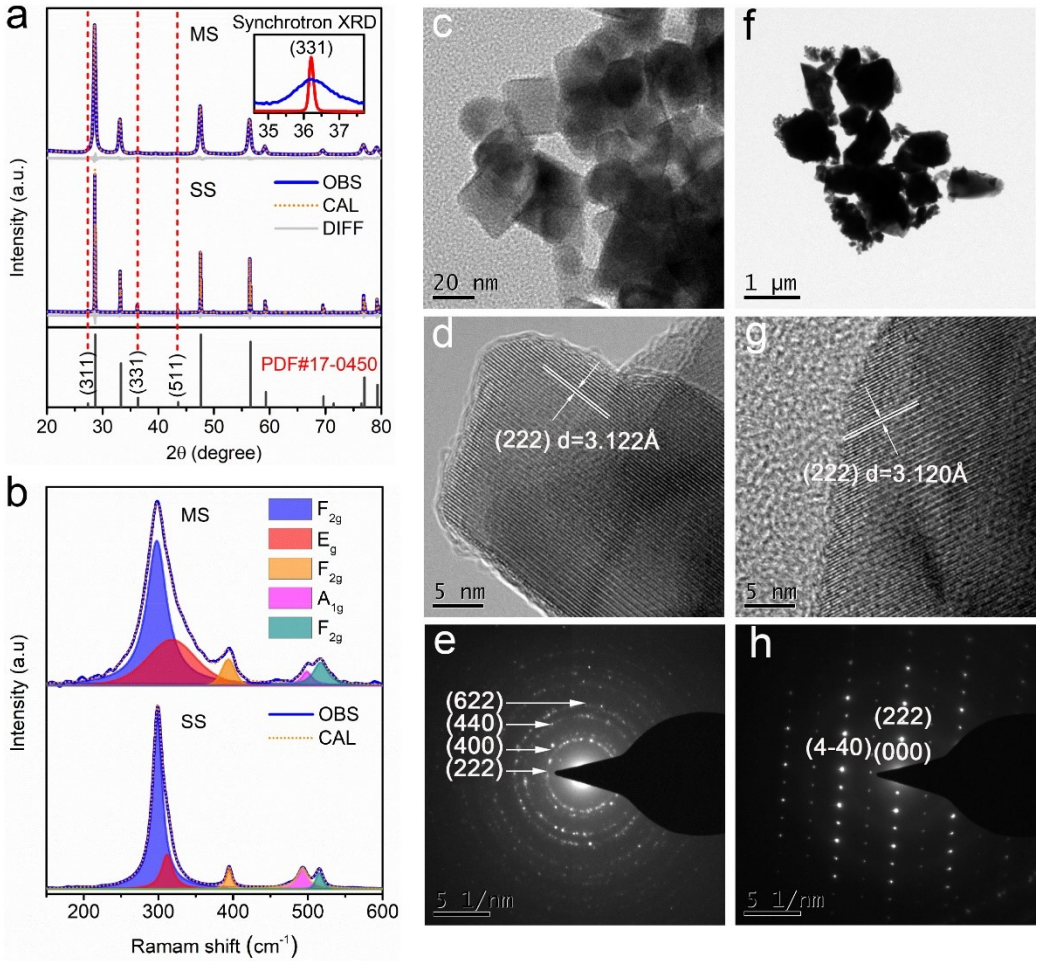

Fig. S1 Structural characterization. (a) The Rietveld refinement of XRD profiles. The magnified view of the diffraction peak corresponding to the (331) plane. (b) Raman spectra of $La_2Zr_2O_7$ by MS method and SS method, respectively (MS refers to molten salt method and SS refers to solid-state method). (c) (d) (e) TEM images of $La_2Zr_2O_7$ by MS method and (f) (g) (h) by SS method.

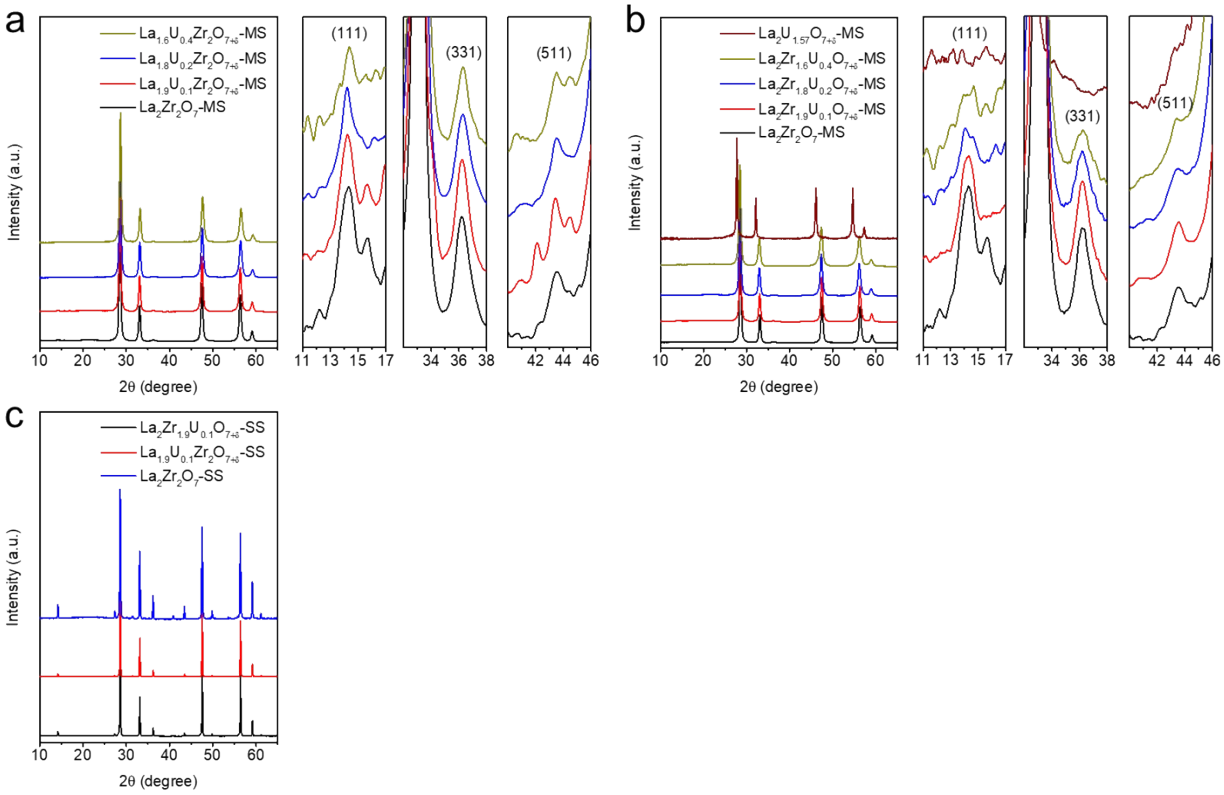

Fig. S2 The Synchrotron XRD patterns for $La_{2-x}U_xZr_2O_{7+\delta}$ and $La_2Zr_{2-y}U_yO_{7+\delta}$ samples. (a) (b) refers to MS method, in which the right panel shows the magnified view of the diffraction peak corresponding to the superlattice peaks (111), (331) and (511). (c) refers to SS method.

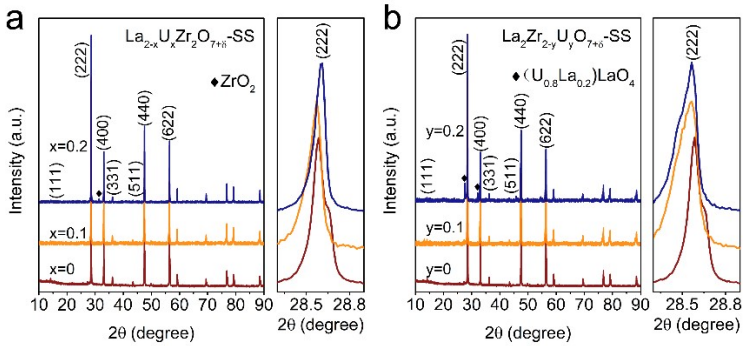

Fig. S3 XRD patterns for (a) $La_{2-x}U_xZr_2O_{7+\delta}$ and (b) $La_2Zr_{2-y}U_yO_{7+\delta}$ samples synthesized by SS method. Along with the magnified view of the diffraction peak corresponding to the (222) plane.

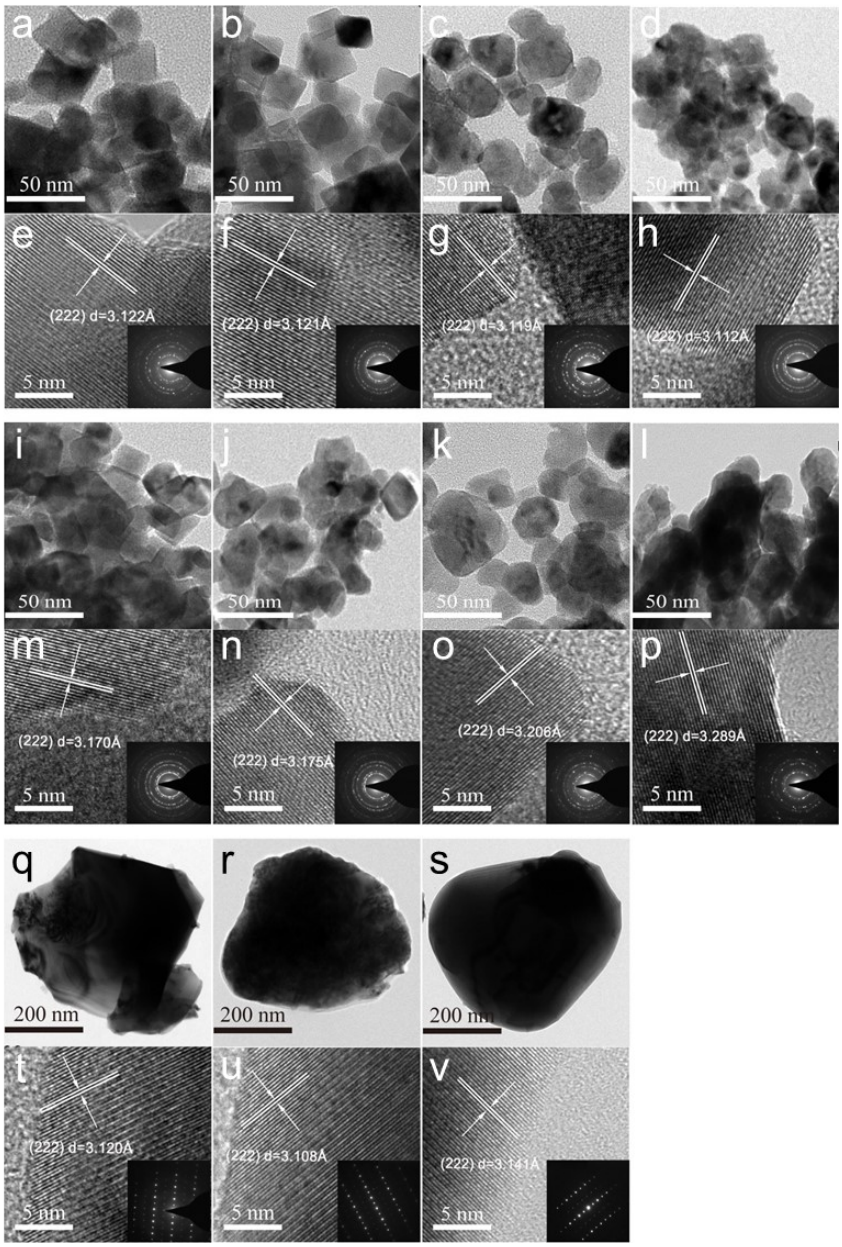

Fig. S4 The TEM images of U-doped $La_2Zr_2O_7$ samples. (a) (e) $La_2Zr_2O_7$-MS, (b) (f) $La_{1.9}U_{0.1}Zr_2O_{7+\delta}$-MS, (c) (g) $La_{1.8}U_{0.2}Zr_2O_{7+\delta}$-MS, (d) (h) $La_{1.6}U_{0.4}Zr_2O_{7+\delta}$-MS, (i) (m) $La_2Zr_{1.9}U_{0.1}O_{7+\delta}$-MS, (j) (n) $La_2Zr_{1.8}U_{0.2}O_{7+\delta}$-MS, (k) (o) $La_2Zr_{1.6}U_{0.4}O_{7+\delta}$-MS, (l) (p)

$La_2U_{1.57}O_{7+\delta}$-MS, (q) (t) $La_2Zr_2O_7$-SS, (r) (u) $La_2Zr_{1.9}U_{0.1}O_{7+\delta}$-SS, (s) (v) $La_2Zr_{1.9}U_{0.1}O_{7+\delta}$-SS. The inset shows the SAED patterns.

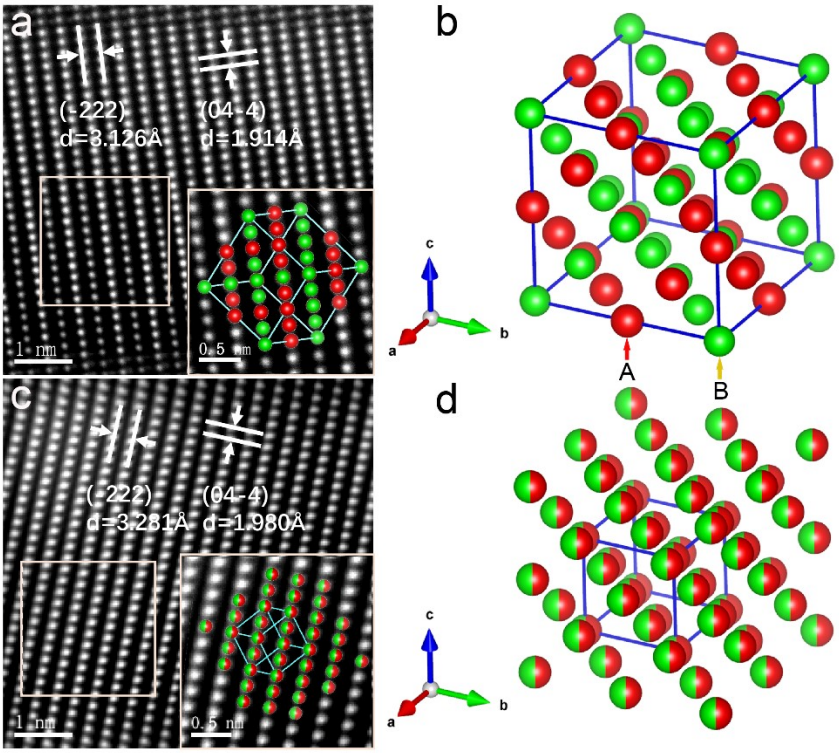

Fig. S5 HAADF-STEM images and their corresponding crystal structure viewed down the [211] axis of $La_2Zr_2O_7$ sample (a, b) and $La_2U_{1.57}O_{7+\delta}$ sample (c, d).

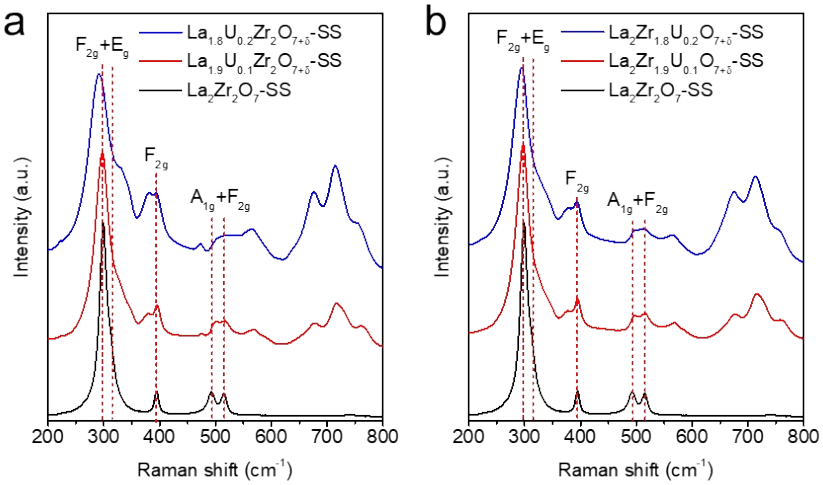

Fig. S6 Raman spectra of $La_{2-x}U_xZr_2O_{7+\delta}$ (a) and $La_2Zr_{2-y}U_yO_{7+\delta}$ (b) samples via SS method.

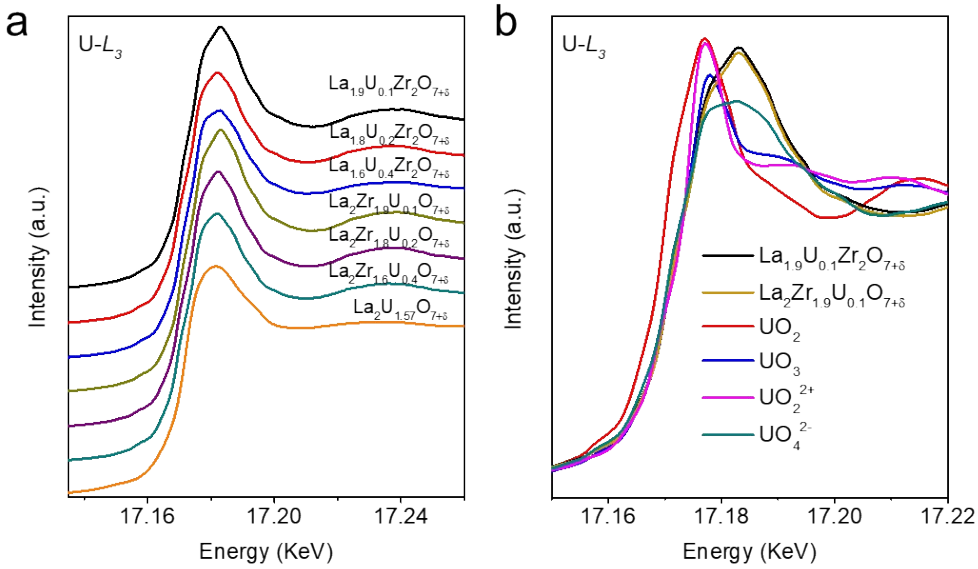

Fig. S7 U-L_3 edge XANES data of all U-doped $La_2Zr_2O_7$ samples along with the standard samples for comparison including UO_4^{2-} ($CoUO_4$), UO_2^{2+} (uranyl nitrate) and UO_3.

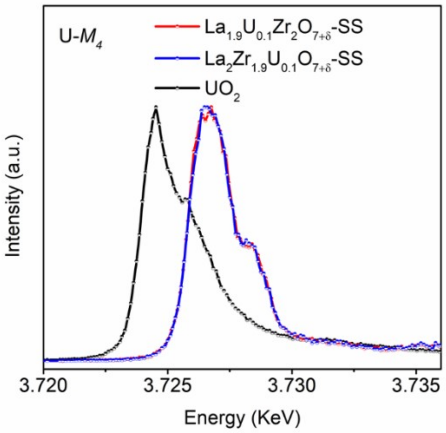

Fig. S8 U-M_4 edge HERFD-XANES data of U-doped $La_2Zr_2O_7$ samples by solid-state method.

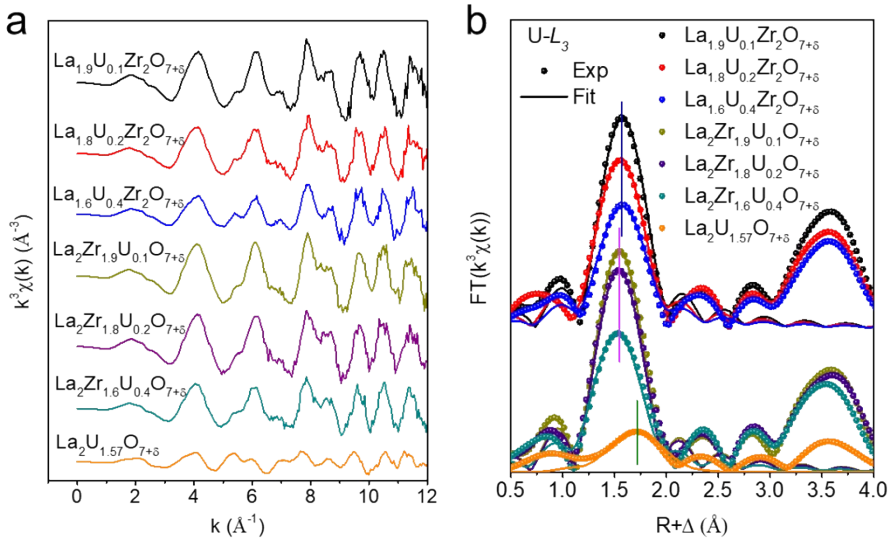

Fig. S9 Spectroscopic data of U doped $La_2Zr_2O_7$-MS sample. (a) k^3-weighted EXAFS spectra at U-L_3 edge. (b) Fourier Transforms data of U-L_3 edge EXAFS data and their corresponding fits.

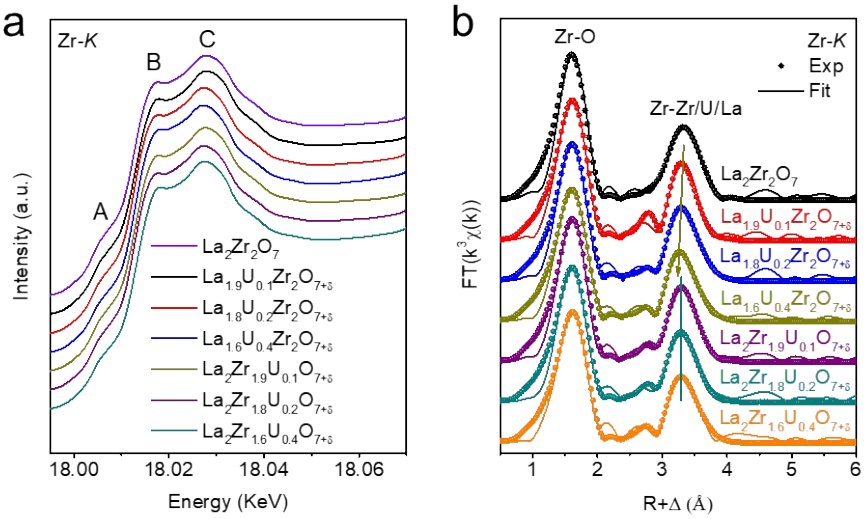

Fig. S10 Spectroscopic data of U doped $La_2Zr_2O_7$-MS samples. (a) Zr-K edge XANES data, (b) Zr-K edge EXAFS spectra in R space and their corresponding fitting data.

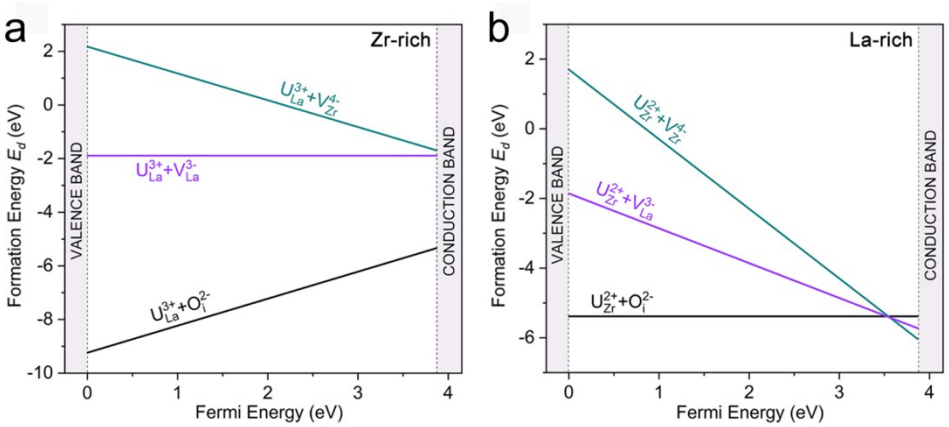

Fig. S11 Formation energies of possible defect pairs under (a) Zr-rich and (b) La-rich condition, as a function of the Fermi energy.

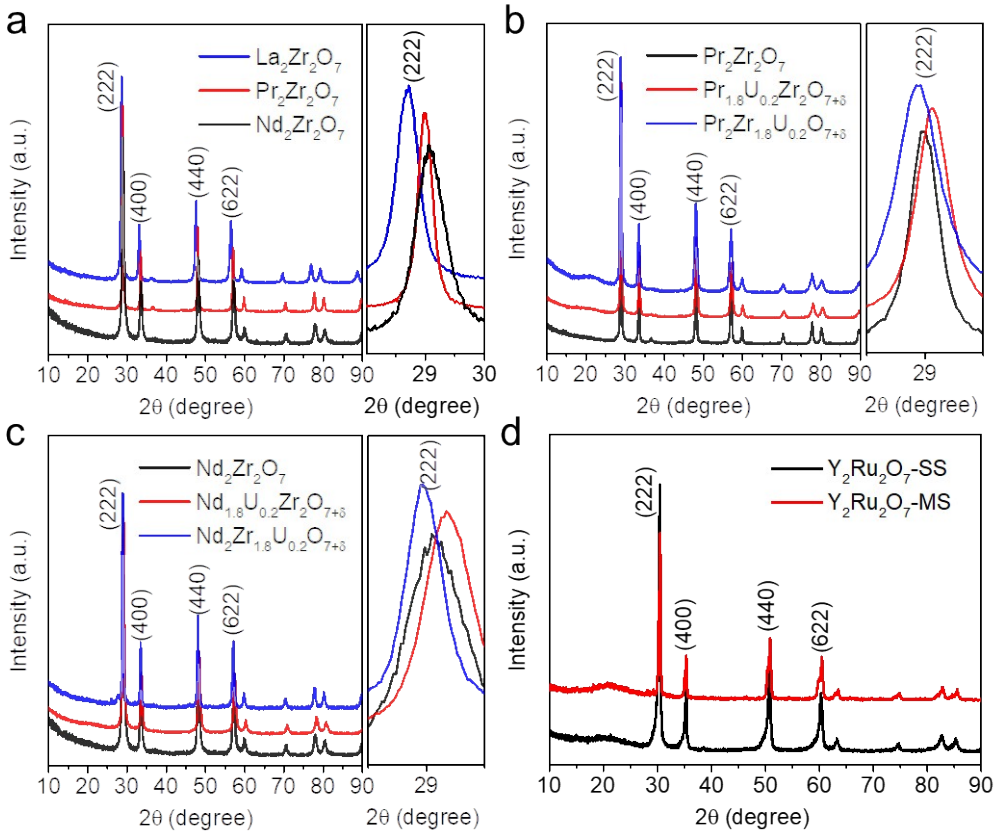

Fig. S12. The XRD pattern of a series of compounds synthesized by molten salt method. (a) A-site substituted zirconate pyrochlore by different lanthanides, (b) uranium doped $Pr_2Zr_2O_7$, (c) uranium doped $Nd_2Zr_2O_7$ and (d) $Y_2Ru_2O_7$ compounds synthesized by molten salt method (850ºC, 6h) and solid-state method (1050 ºC, 12h).

Table S1. Refined structural parameters for $La_{2-x}U_xZr_2O_{7+\delta}$ and $La_2Zr_{2-y}U_yO_{7+\delta}$ samples (Space group: Fd-3m)

Sample	a (Å)	x (O_{48f})	Bond distance (Å)			Rwp	GOF
			La-O_{8b}	La-O_{48f}	Zr-O_{48f}		
$La_2Zr_2O_7$-MS	10.845(1)	0.344(1)	2.348 (1)	2.555 (6)	2.172 (5)	5.22	1.29
$La_{1.9}U_{0.1}Zr_2O_{7+\delta}$-MS	10.841(1)	0.352(1)	2.347 (1)	2.499 (6)	2.213 (5)	5.65	1.40
$La_{1.8}U_{0.2}Zr_2O_{7+\delta}$-MS	10.831(1)	0.351(1)	2.345 (1)	2.508 (7)	2.202 (8)	7.15	1.99
$La_{1.6}U_{0.4}Zr_2O_{7+\delta}$-MS	10.816(1)	0.352(1)	2.342 (1)	2.490 (8)	2.211 (6)	5.06	1.45
$La_{1.4}U_{0.6}Zr_2O_{7+\delta}$-MS	10.720(1)	0.356(1)	2.321 (1)	2.420 (10)	2.232 (10)	12.76	1.42
$La_2Zr_{1.9}U_{0.1}O_{7+\delta}$-MS	10.849(1)	0.351(1)	2.349 (1)	2.503 (8)	2.213 (8)	5.42	1.46
$La_2Zr_{1.8}U_{0.2}O_{7+\delta}$-MS	10.853(1)	0.352(1)	2.350 (1)	2.497 (5)	2.219 (4)	5.54	1.34
$La_2Zr_{1.6}U_{0.4}O_{7+\delta}$-MS	10.858(1)	0.352(1)	2.351 (1)	2.506 (7)	2.214 (6)	7.15	1.91

$La_2U_{1.57}O_{7+\delta}$-MS	11.119(1)	0.353(1)	2.407 (1)	2.629 (12)	——	13.24	1.36
$La_2Zr_2O_7$-SS	10.827(1)	0.332(1)	2.340 (1)	2.639 (5)	2.104 (4)	9.34	1.95
$La_{1.9}U_{0.1}Zr_2O_{7+\delta}$-SS	10.807(1)	0.333(1)	2.340 (1)	2.630 (9)	2.110 (6)	11.92	1.56
$La_{1.8}U_{0.2}Zr_2O_{7+\delta}$-SS	10.809(1)	0.335(1)	2.340 (1)	2.613 (7)	2.121 (8)	13.51	1.73
$La_2Zr_{1.9}U_{0.1}O_{7+\delta}$-SS	10.821(1)	0.331(1)	2.343 (1)	2.646 (8)	2.104 (6)	12.92	1.69
$La_2Zr_{1.8}U_{0.2}O_{7+\delta}$-SS	10.828(1)	0.331(1)	2.344 (1)	2.655 (10)	2.101 (6)	13.27	1.70

Table S2. ICP-MS Data of the $La_2Zr_2O_7$ and the $La_2U_2O_{7+\delta}$ samples.

sample	La (mmol/L)	Zr(mmol/L)	U(mmol/L)	stoichiometry
$La_2Zr_2O_7$	$7.27x10^{-3}$	$7.07x10^{-3}$	———	$La_2Zr_{1.96}O_{7+\delta}$
$La_2U_2O_{7+\delta}$	$4.46x10^{-3}$	———	$3.50x10^{-3}$	$La_2U_{1.57}O_{7+\delta}$

Table S3. Calculated total energy (eV) for defect pairs in $La_2Zr_2O_7$.

Condition	Defect pair	Distance (Å)	Total energy (eV)
Zr-rich	$U_{La}^{3+}+V_{Zr}^{4-}$	3.78	-786.435
		5.38	-785.499
		6.58	-785.282
		9.31	-784.769
	$U_{La}^{3+}+V_{La}^{3-}$	3.83	-797.628
		6.59	-797.340
		7.62	-797.563
		10.09	-797.341
	$U_{La}^{3+}+O_i^{2-}$	4.45	-823.897
		6.70	-823.896

		7.11	-823.928
		7.22	-823.898
La-rich	$U_{Zr}^{2+}+V_{Zr}^{4-}$	6.63	-778.268
		7.66	-778.391
		10.14	-778.269
	$U_{Zr}^{2+}+V_{La}^{3-}$	3.90	-790.346
		6.60	-790.352
		9.38	-790.162
		10.12	-790.346
	$U_{Zr}^{2+}+O_i^{2-}$	2.35	-815.042
		5.9	-815.069
		7.7	-815.069
		11.05	-815.070
	$La_{Zr}^{-}+Zr_{La}^{+}$	3.84	-801.771
		5.44	-801.303
		6.66	-802.008
		9.41	-801.063

Table S4. The SEM-EDS of $La_{2-x}U_xZr_2O_{7+\delta}$ and $La_2Zr_{2-y}U_yO_{7+\delta}$ by MS and SS method.

Sample	Atomic ratio		
	La	Zr	U
$La_2Zr_2O_7$-MS	2	2.14	——
$La_{1.9}U_{0.1}Zr_2O_{7+\delta}$-MS	1.95	2	0.08
$La_{1.8}U_{0.2}Zr_2O_{7+\delta}$-MS	1.89	2	0.19
$La_{1.6}U_{0.4}Zr_2O_{7+\delta}$-MS	1.87	2	0.28
$La_2Zr_{1.9}U_{0.1}O_{7+\delta}$-MS	2	1.67	0.11
$La_2Zr_{1.8}U_{0.2}O_{7+\delta}$-MS	2	1.57	0.21
$La_2Zr_{1.6}U_{0.4}O_{7+\delta}$-MS	2	1.37	0.39
$La_2U_2O_{7+\delta}$-MS	2	——	1.76

$La_2Zr_2O_7$-SS	2	2.16	——
$La_{1.9}U_{0.1}Zr_2O_{7+\delta}$-SS	1.93	2	0.09
$La_{1.8}U_{0.2}Zr_2O_{7+\delta}$-SS	1.87	2	0.21
$La_2Zr_{1.9}U_{0.1}O_{7+\delta}$-SS	2	1.81	0.1
$La_2Zr_{1.8}U_{0.2}O_{7+\delta}$-SS	2	1.79	0.19

7. The chemical potential calculations

As shown in Fig. S11 and Fig. 3, the chemical potential (μ_i) depends on the preparation conditions. A different choice of reference state would modify the relative stability of the investigated U substituting defects. The thermodynamic considerations restrict the accessible range of μ_i if one requires $La_2Zr_2O_7$ stability, which should satisfy the following relationships:

$\mu_o[La_2Zr_2O_7] \leqq \mu_o[O_2]$

$\mu_{La}[La_2Zr_2O_7] \leqq \mu_{La}[metal]$

$\mu_{Zr}[La_2Zr_2O_7] \leqq \mu_{Zr}[metal]$

$7\mu o[La_2Zr_2O_7]+2\mu_{La}[La_2Zr_2O_7]+2\mu_{Zr}[La_2Zr_2O_7] = E(La_2Zr_2O_7)$ (2)

Furthermore, because of the stability of the ternary compound $La_2Zr_2O_7$ against decomposition into its binary oxides La_2O_3 and ZrO_2, the ranges of μ_i are subject to the additional constraints:

$$2\mu_{La}^{La_2O_3}[La_2Zr_2O_7] + 3\mu_O[La_2Zr_2O_7] \leq E(La_2O_3)$$

$$\mu_{Zr}^{ZrO_2}[La_2Zr_2O_7] + 2\mu_O[La_2Zr_2O_7] \leq E(ZrO_2) \quad (3)$$

Under these conditions, we calculated and visualized the range of stable chemical potentials of the components in $La_2Zr_2O_7$, as shown in Fig. S13. The shaded region enclosed by lines connecting points A, B, C, and D indicates the $La_2Zr_2O_7$ stability range, and values outside this region lead to the precipitation of the secondary phases. Lines AD and BC in Fig. S13 correspond to the La_2O_3 (La-rich condition) and ZrO_2 (Zr-rich condition) reference states, respectively. To replicate the experimental conditions, the chemical potential of U should satisfy the requirement for forming its oxide, UO_3:

$\mu_U+3\mu_o= E[UO_3]$ (4)

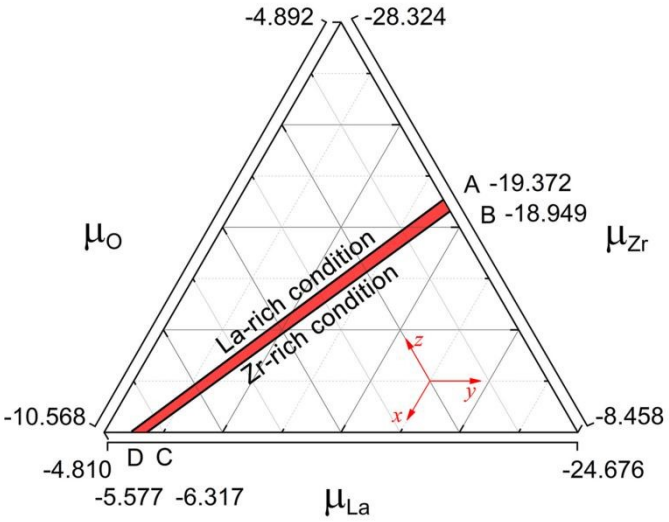

Fig. S13 The stability range of chemical potentials (in eV) of the elements in $La_2Zr_2O_7$. Lines AD and BC correspond to the La_2O_3 and ZrO_2 reference states, respectively. The shaded region enclosed between points A, B, C, and D represents the thermodynamically allowed range of the chemical potentials.

References

1. Y. Mao, X. Guo, J. Y. Huang, K. L. Wang and J. P. Chang, *J. Phys. Chem. C*, 2009, **113**, 1204-1208.
2. G. Kresse and J. Furthmuller, *Phys. Rev. B*, 1996, **54**, 11169-11186.
3. J. P. Perdew, K. Burke and M. Ernzerhof, *Phys. Rev. Lett.*, 1996, **77**, 3865-3868.
4. G. Kresse and D. Joubert, *Phys. Rev. B*, 1999, **59**, 1758-1775.
5. H. J. Monkhorst and J. D. Pack, *Phys. Rev. B*, 1976, **13**, 5188-5192.
6. C. G. Van de Walle and J. Neugebauer, *J. Appl. Phys.*, 2004, **95**, 3851-3879.
7. L. Li, Y. Li and X. Zhao, *Phys. Rev. B*, 2017, **96**, 115118.
8. E. A. Hudson, J. J. Rehr and J. J. Bucher, *Phys. Rev. B*, 1995, **52**, 13815-13826.